Eur. Phys. J. Spec. Top.
https://doi.org/10.1140/epjs/s11734-025-01733-6

THE EUROPEAN PHYSICAL JOURNAL SPECIAL TOPICS

Regular Article

Synthetic generation of additive manufacturing roughness surfaces for computational fluid dynamics using single image data

Thomas Keesom[1,2], Pavel Popov[2], Katherine Hummer[2], Priyank Dhyani[2], and Gustaaf Jacobs[2,a]

[1] Department of Materials Science and Engineering, TU Delft, Delft, The Netherlands
[2] Department of Aerospace Engineering, San Diego State University, San Diego, USA

Received 22 March 2025 / Accepted 4 June 2025

Abstract We present a data-driven method for the synthetic generation of wall roughness of additively manufactured (AM) surfaces. The method adapts Rogallo's synthetic turbulence method (Rogallo in Numerical experiments in homogeneous turbulence, Nasa Technical Memorandum 81315, National Aeronautics and Space Administration, 1981) to generate correlated Fourier modes from data extracted from an electron microscope image. The fields are smooth and compatible with grid generators in computational fluid dynamics or other numerical simulations. Unlike machine learning methods that require more than 20 scans of surface roughness for training, this new method can generate an infinite amount of synthetic roughness fields to any desired spatial domain size, using a single input image. Five types of synthetic roughness fields are tested, based on an input roughness image from literature. A comparison of their spectral energy and two-point correlations shows that a synthetic vector component that aligns with the AM laser path closely approximates the roughness structures of the scan. The synthetic roughness is used in a discontinuous Galerkin laminar boundary-layer simulation, demonstrating the new approach's ease of integration into CFD applications.

1 Introduction

Metal 3D printing techniques such as laser power bed fusion (LPBF) are becoming more widely used in manufacturing. Selective laser melting (SLM), a representative technique within the broad class of LPBF, uses a powder bed of evenly spread metallic powder over a working area, which is fused into the desired shape by locally delivering energy to melt the powder particles together [1, 2]. A well-known disadvantage of this type of Additive Manufacturing (AM) is its rough surface quality. SLM part surfaces, for example, are four-to-five times rougher as compared to machined surfaces [3].

The SLM roughness topography is determined by various physical processes lying at the heart of the manufacturing process [2], including liquefaction of the metal powder, flow instabilities in the liquid metal, the steep cooling rate of the molten powder particles after the delivery of the energy by the laser [4], and others. The manufactured topography, therefore, depends on settings, such as laser input energy, scan speed, scan width, exposure time [5], and the printed object's orientation with respect to the laser [6]. While some reduction of roughness height is possible [5], eliminating the roughness structures is difficult even with additional post-processing techniques [7].

The roughness affects the thermo-fluid dynamics of the flow over an AM surface [8–10], especially if the roughness topography extends beyond flow scales that are relevant to a given problem [11]. Interaction of the flow with the rough wall has been reported to affect mixing processes and heat transfer [12]. The computational prediction of the flow effects has proven challenging thus far: if not properly accounted for, the wall roughness may affect the flow to the point that computational fluid dynamics (CFD) yields meaningless results [13].

Machine learning (ML) approaches have shown promise in the modeling of AM roughness geometries. Khorasini et al. show that artificial neural networks model surface roughness geometries of an SLM created specimen with about half the root-mean-square error compared to the non-ML Poisson and Taguchi method [14]. Fotovvati et al.

[a] e-mail: gjacobs@sdsu.edu (corresponding author)

and La Fé-Perdomo et al. find similar results in a different setting, achieving root-mean-square errors on the order of a few percent when approximating experimental roughness geometry data using ML methods [15]. Akhil et al. compared a range of ML methods to extract statistical image texture features [16].

A disadvantage of ML methods is the requirement of a large amount of data for training. In [14, 15, 17], between 21 and 94 experimental roughness scans are used to train the ML models. The compilation of these data relies on either the existence of a significant database of AM roughness fields of interest, or on access to expensive equipment such as electron microscopes, which is not available to most CFD researchers. Another disadvantage of ML models is that, while they may yield a good approximation of roughness, they will not identify important features which led to that approximation, such as for example non-isotropic autocorrelation.

In this paper, we develop a data-driven model that uses a single electron microscope image to generate synthetic, smooth roughness fields for the purpose of grid generation in numerical simulations. The model is an adaptation of Rogallo's [18] method for initialization of homogeneous turbulence via randomly generated Fourier coefficients with a prescribed energy spectrum. The combination of the Rogallo and Fourier analysis methods brings flexibility well suited for CFD grid generation. Specifically, the roughness domain can take on any regular or irregular shape, and the roughness resolution can vary over the domain. The synthetic roughness is scalable to any desired domain size or topography height, and an infinite amount of surfaces can be generated using a single input roughness image. The roughness generation takes in the order of minutes and the input image is not limited solely to AM roughness or the electron microscopy technique. The method also allows for a systematic study of the connection between the topographical Fourier modes and the modes in the flowfield.

2 Methodology

It is assumed that only a single image of an electron microscope scan of wall roughness is available [here Figure 2(c) of [19] is used]. The red, green, and blue (RGB) colors of each pixel of this image are extracted using the Python package Pillow [20]. The RGB triple is then converted to contour level values as per the colormap included in the electron microscope image, yielding an extracted height data f^E_{lk} for each $(l,\, k)$-th pixel of the image (see Fig. 1a).

The values f^E_{lk} are known at the discrete locations x_l and y_k. Cubic interpolation, which is fourth-order accurate and offers a lower interpolation error compared to linear interpolation, approximates the height, f^I, at the equidistant grid locations $x_i = i\Delta x$ and $y_j = j\Delta y$, where $i = 0,\, 1,\, 2,\, \ldots,\, N-1$ and $j = 0,\, 1,\, 2,\, \ldots,\, M-1$. Then, a Fourier analysis can be performed at the discrete height values, $f^I_{ij} = f^I(x_i,\, y_j)$ on the equidistant grid.

The 2D discrete Fourier transform (DFT) applied to f^I_{ij} yields the Fourier coefficients:

$$\hat{f}^F_{nm} = \frac{1}{NM} \sum_{i=0}^{N-1} \sum_{j=0}^{M-1} f^I_{ij} e^{-k_n x_i \underline{i}} e^{-k_m y_j \underline{i}}, \tag{1}$$

where $k_n = 2\pi n s/L_x$ and $k_m = 2\pi m r/L_y$, with $n = -N/2+1,\, \ldots,\, N/2$ and $m = -M/2+1,\, \ldots,\, M/2$. Here, $L_x = 14\,h$ and $L_y = 8.5h$, where $h = 250\,\mu m$ is the characteristic length scale of the AM roughness in [19]. The scaling factors $s \equiv L_x/2\pi$ and $r \equiv L_y/2\pi$ define the density of the DFT wavenumber spacing.

With the inverse discrete Fourier transform (IDFT), a continuous function is recovered in physical, two-dimensional space

$$f^F(x,\, y) = \sum_{n=-N/2+1}^{N/2} \sum_{m=-M/2+1}^{M/2} \hat{f}^F_{nm} e^{k_n x \underline{i}} e^{k_m y \underline{i}}. \tag{2}$$

To test the overall accuracy of the data extraction procedure, we generate a contour plot of a known analytic roughness and compare the original, known roughness $f^O(x,\, y)$ to the IDFT-generated $f^F(x,\, y)$. For $N = M = 64$ and a high-resolution 1486×1486 image, the relative L^2-error $\varepsilon^F = \frac{\|f^F - f^O\|_2}{\|f^O\|_2}$. is less that 3.11%.

To apply Rogallo's method, we then compute the energy spectrum $E^F(|\mathbf{k}|)$ by integrating the Fourier coefficients over annuli of inner radius $|\mathbf{k}|-1/2$ and outer radius $|\mathbf{k}|+1/2$

$$E^F(|\mathbf{k}|) = \oint \left(\hat{f}_{nm}\right)^2 \mathrm{d}\sigma \approx \sum_{|\mathbf{k}|-0.5 \le \sqrt{k_n^2+k_m^2} < |\mathbf{k}|+0.5} \frac{1}{sr} \left(\hat{f}^F_{nm}\right)^2. \tag{3}$$

$E(|\mathbf{k}|)$ is computed for values of $|\mathbf{k}|$ between 0 and $|\mathbf{k}|_{\max}= \sqrt{\left(\frac{N}{2}\right)^2 + \left(\frac{M}{2}\right)^2}$.

To generate the synthetic roughness height field, Rogallo's method [18] is applied starting with the determination of random numbers whose expected amplitudes follow the energy spectrum according to:

$$\alpha(\mathbf{k}) = \sqrt{\frac{E^F(|\mathbf{k}|)}{\pi|\mathbf{k}|sr}} e^{i\theta}\cos(\Phi), \tag{4}$$

where $\theta \sim U(-\pi, \pi)$, $\Phi \sim U(0, 2\pi)$ are uniform random variables. For divergence-free velocity fields, the Fourier coefficient vector is orthogonal to the wavenumber vector $\boldsymbol{k}$. Thus, in 2D, the Rogallo Fourier coefficient vectors can be specified as

$$\hat{\boldsymbol{f}}^R_{nm}(k_n, k_m) = \begin{bmatrix} \hat{f}^R_n \\ \hat{f}^R_m \end{bmatrix} = \begin{bmatrix} \alpha(\mathbf{k})\frac{k_m}{|\mathbf{k}|} \\ -\alpha(\mathbf{k})\frac{k_n}{|\mathbf{k}|} \end{bmatrix}. \tag{5}$$

These are transformed to the physical space vector

$$\boldsymbol{f}^R = [f^R_x, f^R_y]^T \tag{6}$$

using the IDFT. While $E^F(|\mathbf{k}|)$ is uniquely determined by the single image of the scan, $\alpha(\mathbf{k})$, is a random variable which enables the generation of an arbitrary number of vector fields $\boldsymbol{f}^R$. Moreover, the energy spectrum can be used to extrapolate the synthetic field to much larger areas by increasing the scaling factors s and r in Eq. (4) and the resolution of discrete wavenumbers for which Eq. (5) is applied.

Since the roughness height is a scalar and not a two-dimensional vector, a scalar field has to be extracted from the output of Eq. (6). The x- and y-components, f^R_x and f^R_y, of the vector field $\boldsymbol{f}^R$ are natural choices, as is its magnitude, f^R. The magnitude is a strictly positive scalar, whereas the roughness topography has both positive peaks and negative valleys. On the other hand, the vorticity $f^V = \nabla \times \boldsymbol{f}^R$ of the 2D vector field is symmetric with respect to 0, uses both components of the Rogallo vector field, and is representative of the vector field's topological features as it is in turbulence [21]. The square of the vorticity f^{V^2} (enstrophy) has similar topological representation but for smaller scales. In the results discussed below, we compare the five scalar fields to the scanned roughness images.

3 Results and discussion

3.1 Contour fields

Contours of the extracted f^E roughness and Fourier approximation f^F are plotted in Fig. 1a, b, respectively. A visual inspection shows only small discernable differences between f^F and the original image in [19], which is supported by the small data extraction errors reported in the previous section.

Noting that the local maxima connect with each other to form ridges in the y-direction (which is the laser path direction for that AM sample), whereas the local minima are disjoint and more circular in shape, the qualitative performances of the five scalar fields are assessed based on how well they reproduce these ridges.

The roughness surfaces produced by the components of the synthetic vector field, f^R_x and f^R_y, are presented in Fig. 1c, d, respectively. Both of these surfaces produce ridges whose orientation matches the component direction—the x-component field produces horizontal ridges and the y-component field produces vertical ones similar to those observed in the scanned image (Fig. 1b). It is concluded that the component of the synthetic vector field aligning with the laser path direction yields the better qualitative agreement.

From the contour plot of the magnitude of the synthetic vector field, f^R, (Fig. 1e), it is observed that the local maxima are disjoint and less frequent that in the AM surface, while the minima are more frequent. Overall, a positive skewness (in the statistical sense of that word, namely, the third moment of a random distribution relative to its mean) is observed. This can be attributed to the absolute value in the definition of the field, which increases the probability of values at the lower end of the distribution's range (close to 0 prior to normalization).

The contours of the synthetic vorticity and enstrophy fields, f^V and f^{V^2}, are visualized in Fig. 1f, g, respectively. Again, it is observed that the maxima are disjoint, unlike in the AM scan. We note, however, that the skewness is not as pronounced as in Fig. 1e.

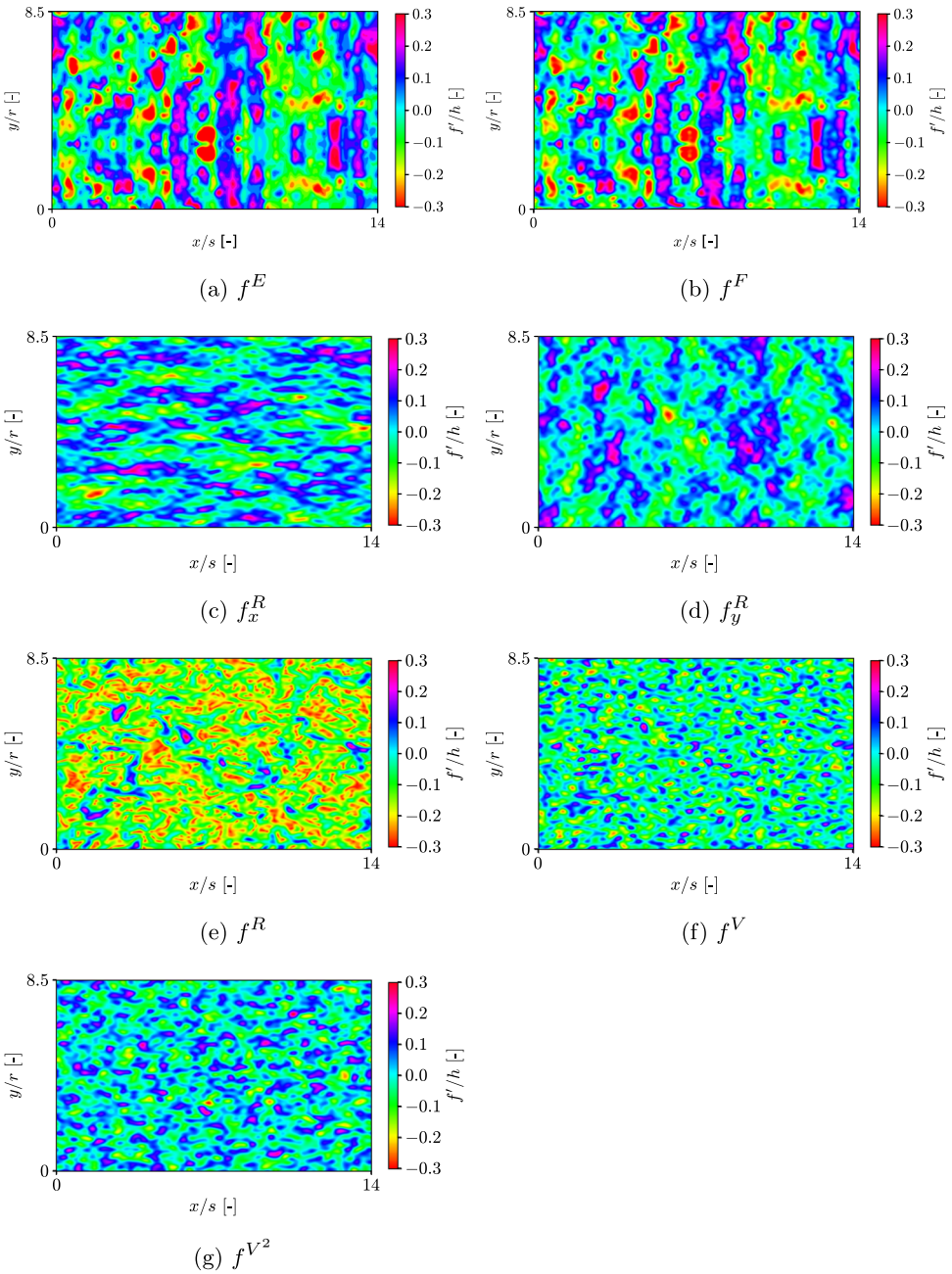

(a) f^E (b) f^F

(c) f_x^R (d) f_y^R

(e) f^R (f) f^V

(g) f^{V^2}

Fig. 1 The extracted f^E, Fourier-Series approximation f^F (plotting resolution 1950×1186, scaling factors $s = 2\pi/14$ and $r = 2\pi/8.5$) of the input roughness surface by Altland et al. [19], and the Rogallo-based synthetic roughnesses derived from it (resolution 500×500, $s = 2\pi/14$ and $r = 2\pi/8.5$)

Based on the qualitative comparisons between contours of the five scalar synthetic fields and the original AM roughness height field, it is concluded that the AM features are best reproduced by f_y^R, the component of the Rogallo vector in the AM laser path direction.

3.2 Statistical characteristics

The statistical accuracy of the representation of the roughness height can be assessed with two-point autocorrelations of the roughness field, which provide information on its spatial structure. For example, below we shall see that the y-direction ridges seen in Fig. 1b, d can be observed in these autocorrelations. The autocorrelations in the x- and y-directions, respectively, $\mathbf{R}_x(\mathbf{r}_x)$ and $\mathbf{R}_y(\mathbf{r}_y)$, are defined by and determined numerically as expressed

by

$$\mathbf{R}_x(\mathbf{r}_x) = \int_0^{L_x} \left(\overline{f(x,\, y) f(x+\mathbf{r}_x,\, y)}\right)' \mathrm{d}x \approx \sum_{i=0}^{N-1} \left(\frac{\overline{f(x_i,\, y_j) f(x_i+\mathbf{r}_x,\, y_j)}}{\overline{f(x_i,\, y_j)}^2} \right) \Delta x,$$

$$\mathbf{R}_y(\mathbf{r}_y) = \int_0^{L_y} \left(\overline{f(x,\, y) f(x,\, y+\mathbf{r}_y)}\right)' \mathrm{d}y \approx \sum_{j=0}^{M-1} \left(\frac{\overline{f(x_i,\, y_j) f(x_i,\, y_j+\mathbf{r}_y)}}{\overline{f(x_i,\, y_j)}^2} \right) \Delta y,$$

where $\mathbf{r}_x$ and $\mathbf{r}_y$ are the separation vectors. The two-point autocorrelations so determined in the x- and y-directions are plotted in Fig. 2a, b, respectively. Only the first half of the correlation functions is shown, since all correlation functions in x and y are symmetric around their midpoint of $\mathbf{r}_x/s = 7.0$ and $\mathbf{r}_y/r = 4.25$, respectively.

We can think of the autocorrelation half-maximum width as a measure of the average size of the roughness structures in the fields. In the x-direction, all fields with the exception of f_x^R have half-maximum widths close to that of f_x^F. Beyond the half-maximum width, for r_x/s, $r_y/r > 1$, the x-two-point correlation becomes negative and then oscillates between -0.1 and 0.1. This negative and oscillatory correlation is caused by the the fact that a line in the x-direction will cross a set of the recurring periodic y-parallel ridges. Consistent with the qualitative observation of the contour fields above, the oscillating behavior of the autocorrelation is best captured by the y-component of the synthetic vector field, f_y^R.

The y-two-point autocorrelation maintains a roughly constant value of 0.2 up to $r_y/r = 4.25$, which is directly related to the ridges of the AM roughness which follow the laser path. In the present case, the laser path is in the y-direction, meaning the roughness height will tend to remain constant in the y-direction (positive correlation plateau). Out of the five synthetic fields, f_y^R captures this behavior best, with a consistently positive R_y with a similar half-maximum width (albeit lower values near $r_y/r = 2$). Additionally, a qualitative comparison of the roughness field contours shows the highest agreement of f_y^R to f^F. This indicates that the optimal Rogallo-based roughness profile is the one based on the component of velocity parallel to the laser's path.

3.3 Size increase and application to CFD

A major benefit of the synthetic roughness method proposed here is that, once $E^F(|\mathbf{k}|)$ is calculated, the size of the Rogallo-based synthetic roughness patch is not limited to the size of the original AM roughness scan. This is demonstrated on Fig. 3, on which we can see a synthetic patch twice the length and height of the original AM scan. Such a size increase is achieved by increasing s, r in Eq. (4) and the corresponding density of Rogallo-generated Fourier modes in Eq. (5).

Additionally, the synthetic roughness process generates Fourier coefficients which can be easily incorporated in analytically defined meshes for CFD simulations with rough walls. This is demonstrated in Fig. 4, which shows contour plots and the mesh of a boundary-layer simulation with synthetic Rogallo roughness. The 2D, non-dimensionalized boundary layer has a Reynolds number $Re = 500$ and a Blasius flat plate initial and inflow boundary condition with $\delta_{99} = 3$; the domain extent is 20×10. A Discontinuous Galerkin (DG) numerical scheme [22] is used, with 60×10 elements, and 5-th-order polynomial reconstruction.

The DG element mesh is shown in Fig. 4c, and a detailed view of the wall region can be seen in Fig. 4d. The bottom boundaries of the first row of elements are fitted to the synthetic roughness produced by the Rogallo method. The horizontal velocity perturbations caused by the roughness are minor relative to the free-stream velocity, and are thus not shown here. The roughness has a much more pronounced effect on the wall-normal velocity, as can be seen in Fig. 4a. The vertical velocity has a positive correlation with the roughness slope, which is to be expected since the boundary-layer velocity is locally parallel to the nearest wall surface.

While v/U_0 at the wall has high frequency components on par with those of the roughness field, we observe that the pressure field seen in Fig. 4b has lower spatial frequencies. This indicates either that the pressure response to the roughness has nonlinear subharmonic interactions, or that it is biased toward the low-frequency modes of roughness. Since the streamwise pressure variation is vital for predicting boundary-layer separation, these results indicate that beyond a simple amplitude, the roughness shape and spectrum may play an essential role in flow separation from AM surfaces.

4 Conclusions

A data-driven model has been developed for the synthetic generation of additive manufacturing (AM) roughness fields based on images of AM roughness electron microscope scans. The method uses data extraction methods, Fourier analysis, and Rogallo's method [18]. The model is well suited for the generation of numerical simulation

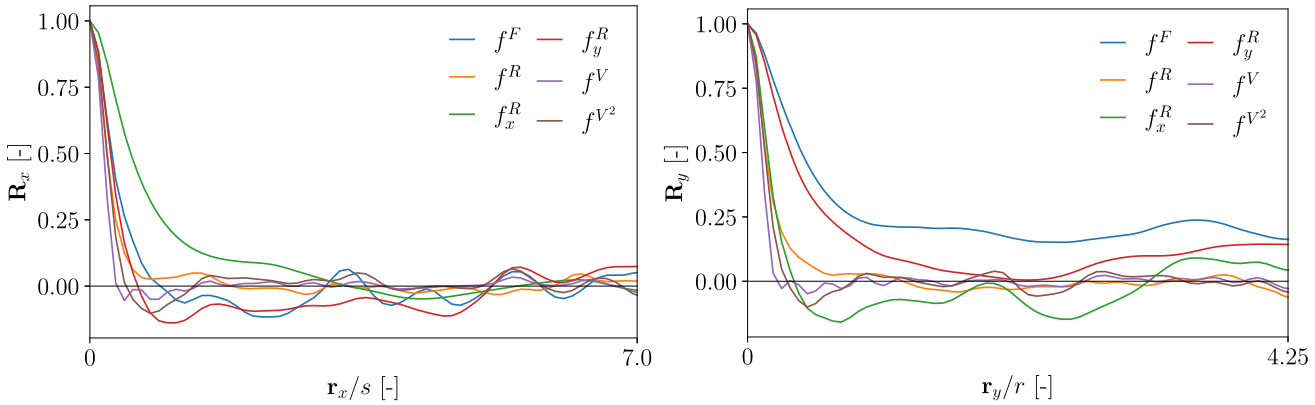

(a) $x-$direction autocorrelation (b) $y-$direction autocorrelation

Fig. 2 Two-point correlation spectra in the x- and y-directions of the AM surface Fourier-Series (FS) approximation and the five synthetic fields

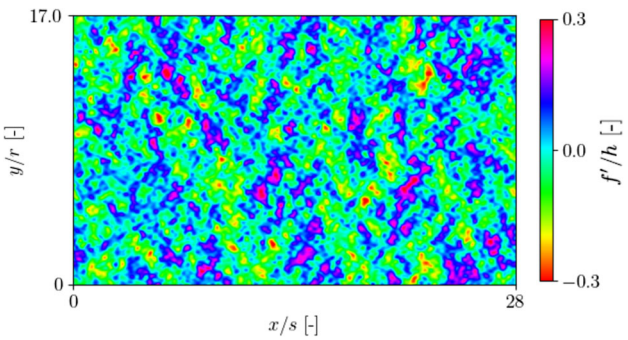

Fig. 3 The y-vector component synthetic roughness field f_y^R, generated over a patch twice the size of the original AM scan

grids with surface roughness. Five synthetically generated roughness fields based on the Rogallo vector field have been tested. Of those five, the one based on the component of the Rogallo vector field parallel to the laser path performs best, capturing anisotropic features such as differing autocorrelation behaviors along the two axes of the surface. The Rogallo-based method requires a single image, unlike the 20+ image datasets needed for training of ML algorithms for synthetic roughness. Thus, the Rogallo roughness based on the laser-path-parallel velocity component is proposed as a superior alternative to existing synthetic roughness models in cases when the existing experimental measurements of AM roughness are limited. It should be noted that so far the method has been applied only to AM roughness which is in the horizontal plane of the 3D printer, with uniform laser path directions. Thus, further work may be needed to make it applicable to different AM roughness orientations, and to AM manufacturing methods in which the laser path direction varies along the component's shape.

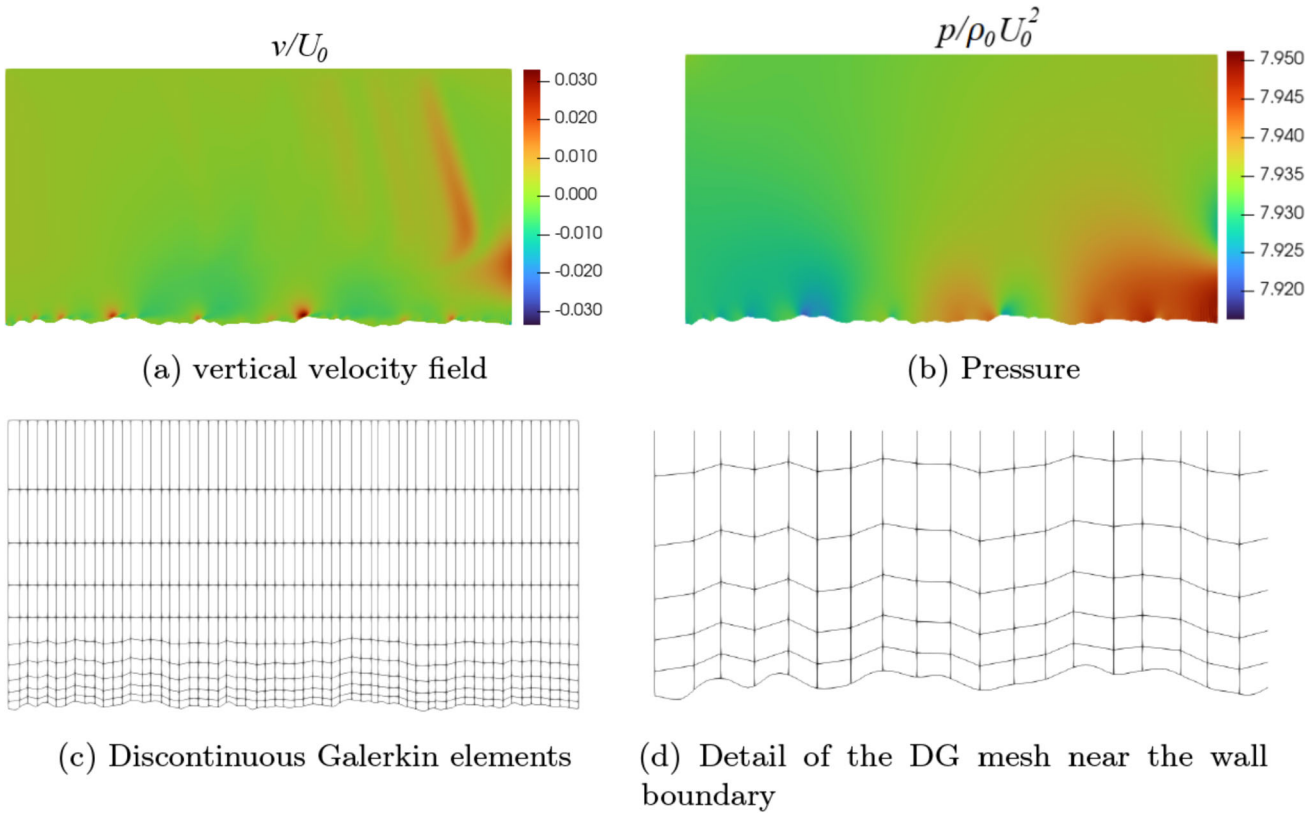

Fig. 4 Use of the synthetic roughness field for wall boundary specification in simulations of flow over an AM surface

Acknowledgements This work is supported by the National Energy Technology Laboratory's University Turbine Systems Research Program, DE-FOA-0002397.

Data availability Code and data will be made available upon a reasonable request.

References

1. W.E. Frazier, Metal additive manufacturing: a review. J. Mater. Eng. Perform. **23**(6), 1917–1928 (2014)
2. A. Bouabbou, S. Vaudreuil, Understanding laser-metal interaction in selective laser melting additive manufacturing through numerical modelling and simulation: a review. Virtual Phys. Prototyp. **17**(3), 543–562 (2022)
3. T.M. Mower, M.J. Long, Mechanical behavior of additive manufactured, powder-bed laser-fused materials. Mater. Sci. Eng. A **651**, 198–213 (2016)
4. N.T. Aboulkhair, M. Simonelli, L. Parry, I. Ashcroft, C. Tuck, R. Hague, 3D printing of aluminium alloys: additive manufacturing of aluminium alloys using selective laser melting. Prog. Mater Sci. **106**, 100578 (2019)
5. E. Abele, M. Kniepkamp, Analysis and optimisation of vertical surface roughness in micro selective laser melting. Surf. Topogr. Metrol. Prop. **3**(3), 034007 (2015)
6. J.C. Fox, S.P. Moylan, B.M. Lane, Effect of process parameters on the surface roughness of overhanging structures in laser powder bed fusion additive manufacturing. Procedia CIRP **45**, 131–134 (2016)
7. G. Favero, G. Berti, M. Bonesso, D. Morrone, S. Oriolo, P. Rebesan, R. Dima, P. Gregori, A. Pepato, A. Scanavini, S. Mancin, Experimental and numerical analyses of fluid flow inside additively manufactured and smoothed cooling channels. Int. Commun. Heat Mass Transf. **135**, 106128 (2022)
8. K.C. Chen, Compressible turbulent boundary-layer heat transfer to rough surfaces in pressure gradient. AIAA J. **10**(5), 623–629 (1972)
9. R.A. Antonia, R.E. Luxton, The response of a turbulent boundary layer to a step change in surface roughness part 1. Smooth-to-rough. J. Fluid Mech. **48**, 721–761 (1971)
10. R.A. Antonia, R.E. Luxton, The response of a turbulent boundary layer to a step change in surface roughness. Part 2. Rough-to-smooth. J. Fluid Mech. **53**, 737–757 (1972)
11. D.V. Brezgin, K.E. Aronson, F. Mazzelli, A. Milazzo, The surface roughness effect on the performance of supersonic ejectors. Thermophys. Aeromech. **24**(4), 553–561 (2017)

12. C. Gramespacher, H. Albiez, M. Stripf, H.J. Bauer, The influence of element thermal conductivity, shape, and density on heat transfer in a rough wall turbulent boundary layer with strong pressure gradients. J. Turbomach. **143**(8), 9 (2021)
13. S.T. McClain, D.R. Hanson, E. Cinnamon, J.C. Snyder, R.F. Kunz, K.A. Thole, Flow in a simulated turbine blade cooling channel with spatially varying roughness caused by additive manufacturing orientation. J. Turbomach. Trans. ASME **143**(7), 12 (2021)
14. A.M. Khorasani, I. Gibson, M. Goldberg, G. Littlefair, A comprehensive study on surface quality in 5-axis milling of SLM Ti-6Al-4V spherical components. Int. J. Adv. Manuf. Technol. **94**(9–12), 3765–3784 (2018)
15. B. Fotovvati, S. Rauniyar, J.A. Arnold, K. Chou, Experimental, computational, and data-driven study of the effects of selective laser melting (SLM) process parameters on single-layer surface characteristics. Int. J. Adv. Manuf. Technol. **123**(1–2), 119–144 (2022)
16. V. Akhil, G. Raghav, N. Arunachalam, D.S. Srinivas, Image data-based surface texture characterization and prediction using machine learning approaches for additive manufacturing. J. Comput. Inf. Sci. Eng. **20**(2), 021010 (2020)
17. I. La Fé-Perdomo, J.A. Ramos-Grez, I. Jeria, C. Guerra, G.O. Barrionuevo, Comparative analysis and experimental validation of statistical and machine learning-based regressors for modeling the surface roughness and mechanical properties of 316l stainless steel specimens produced by selective laser melting. J. Manuf. Process. **80**, 666–682 (2022)
18. R.S. Rogallo, Numerical experiments in homogeneous turbulence. Nasa Technical Memorandum 81315, National Aeronautics and Space Administration (1981)
19. S. Altland, X. Zhu, S. McClain, R. Kunz, X. Yang, Flow in additively manufactured super-rough channels. Flow **2** (2022)
20. F. Lundh, A. Clark, Pillow. https://pillow.readthedocs.io/en/stable/index.html. Accessed: 11/14/2022
21. F.T.M. Nieuwstadt, B.J. Boersma, J. Westerweel, *Turbulence: Introduction to Theory and Applications of Turbulent Flows* (Springer, Cham, 2016)
22. B.F. Klose, G.B. Jacobs, D.A. Kopriva, Assessing standard and kinetic energy conserving volume fluxes in discontinuous Galerkin formulations for marginally resolved Navier-Stokes flows. Comput. Fluids **205**, 104557 (2020)